THE ISOTHERMAL OUTFLOW IN THE MASSIVE STAR-FORMING REGION G240.31+0.07

Junhao Liu,[1] Keping Qiu,[1, 2] Friedrich Wyrowski,[3] Karl Menten,[3] and Rolf Güsten[3]

[1]School of Astronomy and Space Science, Nanjing University, 163 Xianlin Avenue, Nanjing 210023, P.R.China
[2]Key Laboratory of Modern Astronomy and Astrophysics (Nanjing University), Ministry of Education, Nanjing 210023, P.R.China
[3]Max-Planck-Institut für Radioastronomie, Auf dem Hügel 69, 53121 Bonn, Germany

ABSTRACT

We present Atacama Pathfinder Experiment (APEX) observations toward the massive star-forming region G240.31+0.07 in the CO (3-2), (6-5), and (7-6) lines. These lines have traced the previously detected bipolar outflow and show similarity in morphology. The CO (3-2), (6-5), and (7-6) data were complemented with previously observed CO (2-1) data. All line ratios of the four transitions are remarkably constant with velocity. Using the CO (3-2), (6-5), and (7-6) data and the complementary CO (2-1) data, we estimate the physical parameters of the outflow as functions of the gas velocity, by the means of the rotalation diagram analysis and the large velocity gradient (LVG) analysis. Our analysing results reveal that the the outflow is isothermal and has a temperature of ~ 50 K. This value is warmer than previously adopted ~ 30 K. We also find a decreasing trend of CO column density with gas velocity. In addition, the modeling results reveal that the outflowing gas is thermalized and has gas densities of $> 10^5$ cm^{-3}. A decreasing trend of gas density with velocity is detected if assumptions of a constant CO abundance ratio and a constant velocity gradient are valid. The isothermal state and the decreasing density-velocity trend are qualitatively consistent with the wide-angle wind-driven model. Since wide-angle winds associated with low-mass YSOs are related to disk-accretion process, the wide-angle wind-driven G240 outflow provides evidence that high-mass stars up to late-O types can form via disk-mediated accretion.

Keywords: ISM: individual objects (G240.31+0.07) - ISM: jets and outflows - stars: formation

1. INTRODUCTION

Bipolar molecular outflows, mostly observed via CO, HCO$^+$ and their isotopes, are a common phenomenon associated with young stellar objects (YSOs) of all masses (Zhang et al. 2001; Beuther et al. 2002a; Wu et al. 2004, 2005; Maud et al. 2015). It is believed that molecular outflows trace the accretion-powered ejections in sites of low-mass star formation. As molecular outflows impact the surrounding material and the parent cloud significantly, they play an important role in the star formation process. Though molecular outflows have been well studied, the driving mechanism of molecular outflows remains unknown. Molecular outflows from low-mass protostars were thought to be entrained by wide-angle winds (Shu et al. 1991; Lee et al. 2001), or by jet bow shocks (Raga & Cabrit 1993; Masson & Chernin 1993; Lee et al. 2001). Though the wind-driven model

and the jet-driven model can each explain the characteristics of some observed outflows, none of them are capable of producing the observed features of all types of outflows (Lee et al. 2000, 2002). In order to explain different features of various types of outflows associated with low-mass YSOs simultaneously, two-component models with both highly collimated jet and wide-angle wind have been developed (Shu et al. 2000; Banerjee & Pudritz 2006; Pudritz et al. 2006; Shang et al. 2006; Pudritz et al. 2007; Machida et al. 2008).

Massive molecular outflows are more problematic than their low-mass counterparts. Though observations have shown that the morphology and kinematics of some outflows driven by massive sources are very similar to the outflows driven by low-mass YSOs (Shepherd et al. 1998; Beuther et al. 2002b; Qiu et al. 2009; Ren et al. 2011), there is a lack of detection of extremely collimated outflows and circumstellar disks towards sources more massive than early B-type sources (Arce et al. 2007). Thus, it is not clear whether massive stars form as a scaled-up version of low-mass stars or they form in a different

Corresponding author: Keping Qiu
kpqiu@nju.edu.cn

way. Due to the rarity and typically large distances of high-mass sources, the sample of individual studies towards outflows driven by massive sources is still small. And there is little theoretical work on modeling outflows from high-mass sources. Many questions, e.g., how the outflows from massive sources are accelerated, how they differ from low-mass outflows, and how they affect the high-mass star-forming processes, are still unanswered. It is essential to address these questions by studying more outflows associated with high-mass star-forming regions.

Most previous studies of outflows have used low-J rotational transitions of CO (transitions up to $J_u = 3$, with upper-state energies E_u up to 30 K), which are easily excited at low temperatures, to characterize the relatively cold and extended molecular gas in morphology and kinematics. These low-J CO emission lines can be easily observed from the ground-based facilities. Due to atmospheric limits, mid-J CO lines (referring to CO (6-5) and CO (7-6) throughout this paper, with E_u up to 150 K), which are less affected by ambient gas, are not commonly observed. In several studies, mid-J CO transitions have been reported to trace the warm gas (T > 50 K) in outflows of low-mass and intermediate-mass YSOs (van Kempen et al. 2009a,b; Yıldız et al. 2012; van Kempen et al. 2016). By comparing multi-line CO observations (both low-J and mid-J) with the results of non-LTE radiative transfer models, the physical properties (temperature, gas density and CO column density) of the outflowing gas could be well constrained (Lefloch et al. 2015).

This paper is a follow-up study of the G240.31+0.07 (hereafter G240) outflow (Qiu et al. 2009). We report the 12-m submillimeter Atacama Pathfinder Experiment Telescope[1] (APEX) observations of G240, an active high-mass star-forming region which is associated with the source IRAS 07427-2400 and located at a distance of 5.41 kpc (Sakai et al. 2015). It harbors an ultracompact HII region and is associated with OH and H_2O masers (Hughes & MacLeod 1993; Caswell 1997; MacLeod et al. 1998; Migenes et al. 1999; Caswell 2003). Its far-infrared luminosity of $10^{4.7}$ $L_{\odot}$ is consistent with a spectral type O8.5 zero-age main-sequence star (MacLeod et al. 1998). Qiu et al. (2009) presented a high resolution interferometric study at 1.3 mm and resolved the central part of G240 into three dusty cores MM1, MM2, and MM3. Kumar et al. (2003) mapped

the CO (3-2) emission with a $20''$ beam and found a prominent bipolar outflow at a position angle (PA) of $132°$ and a weaker component at PA $\sim 101°$. With $C^{18}O$ (2-1) observations, Kumar et al. (2003) found the cloud velocity (v_{cloud}) with respect to the local standard of rest to be ~ 67.5 km s^{-1}. Recently, Qiu et al. (2009) presented a detailed single dish and interferometric study of ^{12}CO (2-1) and ^{13}CO (2-1) emissions and detected a bipolar, wide-angle, quasi-parabolic molecular outflow. In addition, Qiu et al. (2014) reported the detection of an hourglass magnetic field aligned within $20°$ of the outflow axis.

In this paper, we present a CO multi-transition (2-1, 3-2, 6-5, 7-6) study towards the G240 outflow. With rotation diagram (RD) analysis and large velocity gradient (LVG) calculations, we estimate the physical parameters of the outflow as functions of gas velocity. We then discuss the results of the analysis.

2. OBSERVATIONS

The observations were performed with the 12 m APEX telescope. The CO (3-2) tansition was observed in 200? using the ? receiver, whereas the CO (6-5) and CO (7-6) lines were observed simultaneously in 2009 with the CHAMP+ receiver. Pointings were checked by comparing these lines with the CO (2-1) data adopted from Qiu et al. (2009), and were found to be within $\sim 7''$ for CO (3-2) and within $\sim 4''$ for CO (6-5) and (7-6). The system temperatures were found to be ? at ? GHz. The ? spectrometer was used as the backend with a resolution of ? kHz (? km s^{-1}). The data were smoothed to 2 km s^{-1}, then the rms noises in the spectra in the central part of the map are of the order 0.03-0.05 K at 345 GHz, 0.15-0.25 K at 691 GHz and 0.40 - 0.60 K at 809 GHz at the central region of the maps. Noises are higher at the edge of the maps. Beam efficiencies, determined by observations of planets, were 0.65, 0.41 and 0.40 at 345 GHz, 691 GHz and 809 GHz, respectively. The APEX beam sizes are $\sim 19''$ at 345 GHz, $\sim 9''$ at 691 GHz and $\sim 8''$ at 809 GHz. Calibration uncertainties were assumed to be 15 %, 20% and 30% at 345 GHz, 691 GHz and 809 GHz, relatively. These data were complemented with the perviously observed combined data from the Submillimeter Array[2] (SMA) and the Caltech Submillimeter Observatory[3] (CSO) 10.4 m telescope in CO (2-1) (Qiu et al. 2009). The CO (2-1)

Table 1. Line informations

Line	Frequency	Beam size	σ_{cal} [a]	σ_{rms} [b]	η_s [c]
	GHz	"	%	K	
CO (2-1)	230.5380	3.93×3.10 [d]	10	0.08	–
CO (3-2)	345.7960	19.16	15	0.04	0.65
CO (6-5)	691.4731	9.49	20	0.20	0.41
CO (7-6)	806.6518	8.12	30	0.50	0.40

[a] Calibration error.

[b] Average rms in 2 km s^{-1} channels.

[c] Beam efficiency.

[d] Major axis × minor axis.

data has a calibration uncertainty of 10 %, with the rms estimated to be 0.06-0.10 K in 2 km s^{-1} channels. Table 1 shows a summary of the line informations.

3. RESULTS

3.1. *CO emission maps*

The CO (3-2), (6-5) and (7-6) emissions are detected (with obvious outflow signatures and with peak intensities $> 2\ \sigma_{rms}$) in velocity ranges from 42 km s^{-1} to 94 km s^{-1}, 44 km s^{-1} to 92 km s^{-1}, and 46 km s^{-1} to 90 km s^{-1}, respectively. Figure 1 shows the integrated low-velocity (LV) and high-velocity (HV) emissions of the four lines. The velocity ranges chosen to highlight the LV and HV components of the outflowing gas follow those in Qiu et al. (2009), except that channels with no detections were excluded for the HV component. The morphologies of the bipolar outflow seen in CO (3-2), (6-5) and (7-6) emissions are very similar. Due to the limit of angular resolution, the wide-angle structure highlighted by the CO (2-1) emission is not seen in the CO (3-2), (6-5), (7-6) maps.

3.2. *Physical conditions of the outflow*

3.2.1. *Methodology*

The physical conditions of the outflow could be constrained by comparing the observed line intensities with results of statistical-equilibrium calculations. To study the four lines at the same spatial resolution, we convolved the CO (2-1), (6-5) and (7-6) maps to the same beam size of the CO (3-2) map. The average rms noises are 0.004 K, 0.04 K and 0.10 K for the convolved CO (2-1), (6-5) and (7-6) data, respectively. For following analysis, the CO line intensities were then measured at roughly the peak positions of the HV components of the bluelobe and redlobe of the convolved CO maps (marked

as two crosses in each panel of Figure 1). Figure 2 shows the observed ratios of main-beam temperatures (T_{mb}) of different CO lines of as functions of velocity. Up to $\sim \pm$ 25 km s^{-1} with respect to the cloud velocity, the line ratios are remarkably constant with velocity. To avoid contaminations from the ambient gas, we limited our analysis to velocity ranges of ≤ 60 km s^{-1} and ≥ 74 km s^{-1}. And we restricted our analysis to velocities ranges with high signal-to-noise ratios in ≥ 46 km s^{-1} and ≤ 90 km s^{-1}. Considering that the ^{13}CO (2-1) emission was only marginally detected in the outflowing gas with high sensitivity observations (Qiu et al. 2009), we assumed the four ^{12}CO lines to be optically thin during our analysis. Both the calibration error and the rms noise were taken into account in the belowing analysis.

3.2.2. *Rotation diagram analysis*

Firstly, we performed a simple rotation diagram (RD) analysis (Goldsmith & Langer 1999) to estimate the excitation conditions of the outflowing gas in each 2 km s^{-1} velocity interval under the assumption of local thermal equilibrium (LTE). We didn't correct our observed intensities with beam-filling factors. Thus, the derived physical parameters are values averaged over the beam. The population of each level is given by

$$N_{up} = \frac{N_{CO}}{Z} g_{up} e^{-E_{up}/kT_{kin}}, \qquad (1)$$

where N_{up} is the column density in the upper state, g_{up} the statistical weight of the upper state, E_{up} the upper energy level, k the Boltzmann constant, and Z is the partition function. The rotation diagram for CO at 84 km s^{-1} is shown in Figure 3 as an example. Similar rotation diagrams were found at other velocities. It should be noted that the different energy levels in each velocity bin could be well reproduced with a single-component excitation condition, indicating that the four transitions probe the same volume of gas.

#### 3.2.3. *Large velocity gradient analysis*

Secondly, the non-LTE radiative transfer code RADEX (van der Tak et al. 2007) was used to better constrain the gas density (n_{H_2}), the kinetic temperature (T_{kin}) and the CO column density (N_{CO}) of the outflowing gas in each 2 km s^{-1} bin in the Large Velocity Gradient (LVG) approximation. We built a large grid of LVG models varying the three parameters (n_{H_2}, T_{kin} and N_{CO}), and the best fitting results were then obtained by minimizing the χ^2 between the observed intensities and the model intensities. With four lines observed and three parameters to constrain, our fitting had one degree of freedom. In Figure 4, the fitting results at 84 km s^{-1} are shown as examples of the χ^2 distributions.
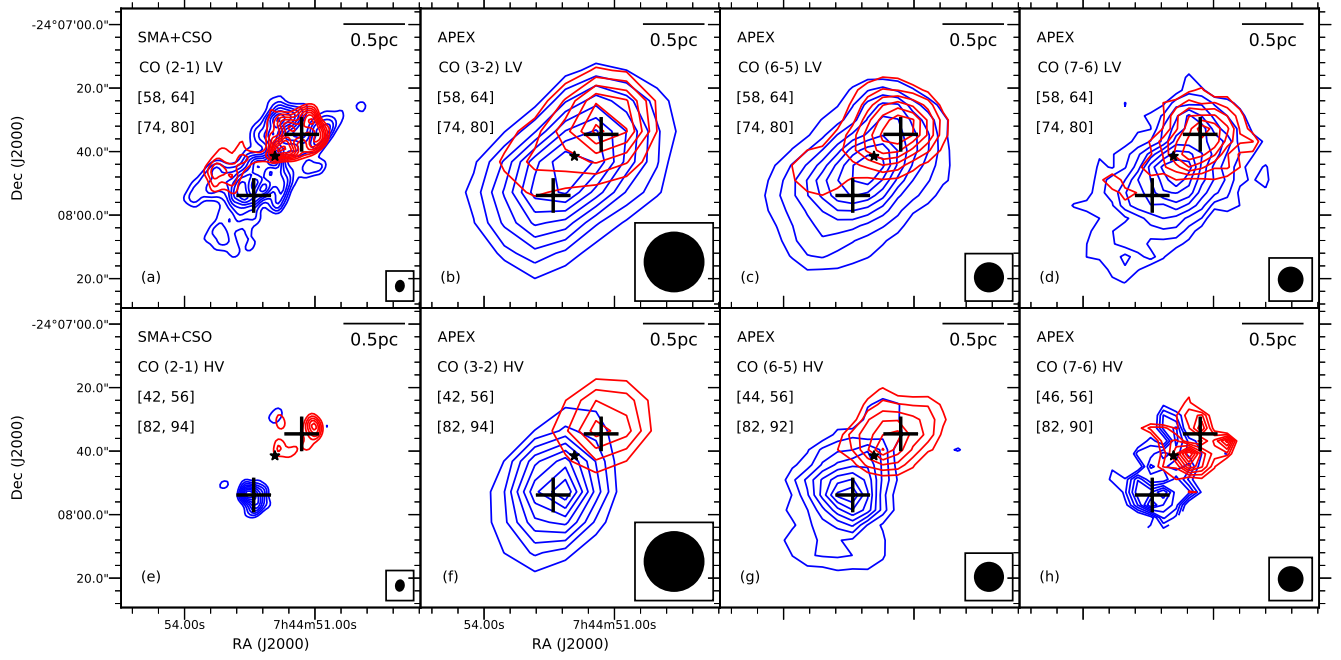
Figure 1. (a)-(d) Low-velocity CO J = (2-1), (3-2), (6-5), (7-6) emissions, integrated from 58 to 64 km s^{-1} for the blueshifted lobe (blue) and from 74 to 80 km s^{-1} for the redshifted lobe (red); (e)-(f) High-velocity CO J = (2-1), (3-2) emissions, integrated from 42 to 56 km s^{-1} for the blueshifted lobe (blue) and from 82 to 94 km s^{-1} for the redshifted lobe (red); (g) High-velocity CO J = (6-5) emission, integrated from 44 to 56 km s^{-1} for the blueshifted lobe (blue) and from 82 to 92 km s^{-1} for the redshifted lobe (red) (h) High-velocity CO J = (7-6) emission, integrated from 46 to 56 km s^{-1} for the blueshifted lobe (blue) and from 82 to 90 km s^{-1} for the redshifted lobe (red). For (a)-(g), the contour levels start from 20% and continue at steps of 10% of the peak emission. For (h), the contour levels start from 30% and continue at steps of 10% of the peak emission. Edge channels are masked out because of high noise levels. The black star marks the position of a H$_2$O maser spot which is associated with IRAS 07427-2400 (Sakai et al. 2015). The beam of each observational dataset is shown in the lower right corner of each panel.
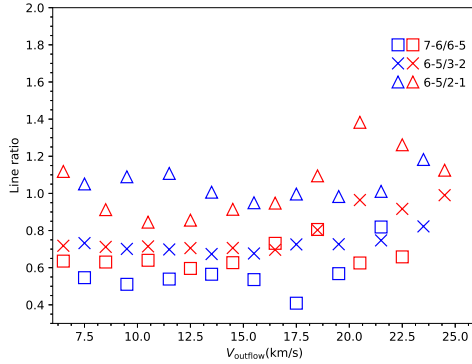

Figure 2. Ratios of main-beam temperatures of different CO lines at different velocities. Blue symbols denote the measurements from the blueshifted lobe, and red symbols the redshifted lobe. The V_{outflow} shown here is related to the cloud velocity v_{cloud} by the relation: $V_{\mathrm{outflow}} = |\ v_{\mathrm{outflow}} - v_{\mathrm{cloud}}|$, where v_{outflow} is the outflow velocity with respect to the local standard of rest.
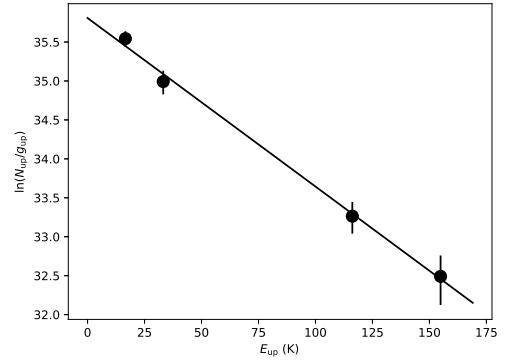
Figure 3. A rotation diagram for CO at 84 km s^{-1}. The fitted line shows the Boltzmann distribution of the rotational populations. The black solid circles show the data with error bars.

Only one minimum of χ^2 is found in the $[T, N]$ plane. In the $[T, n]$ and $[n, N]$ planes, the χ^2 distribution show that the gas is thermalized and no upper limits to

(a)

(b)

(c)
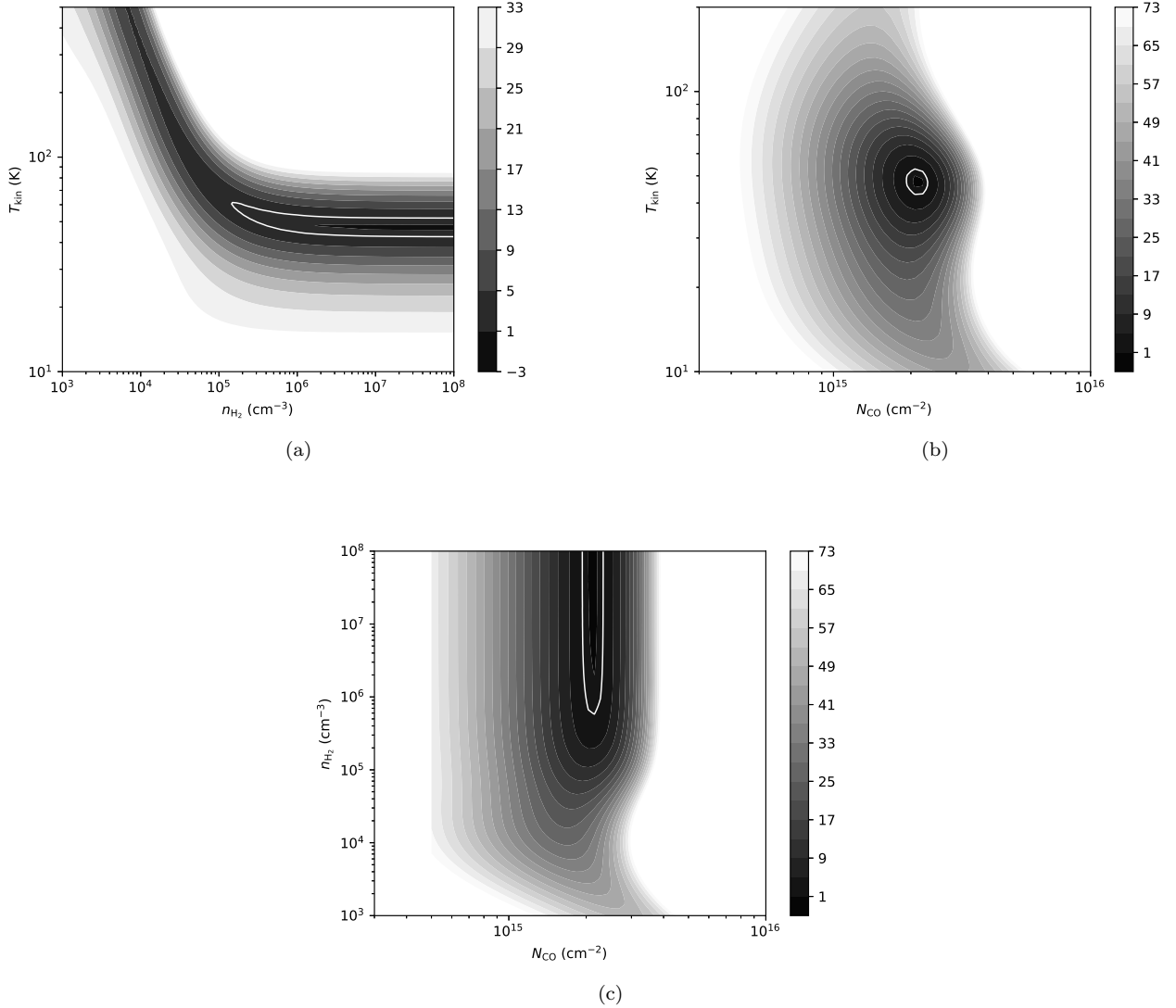
Figure 4. (a)-(c) The χ^2 distribution at 84 km s^{-1} in the $[T, n]$, $[T, N]$ and $[n, N]$ planes, with all other parameters fixed to the values of the best fitting results at this velocity. The $\chi^2_{\rm red}$ of the best fitting result is 1.00 at 84 km s^{-1}. The Solid white contours show the 1σ confidence levels.

the density could be derived, which confirms the LTE assumption of the rotation diagram analysis. Similar χ^2 distribution profiles were found at other velocities. The reduced χ^2 ($\chi^2_{\rm red}$) of the best fitting results varies from 0.10 to 1.72 at different velocities. We derive the uncertainties of each parameter of the fitting results from the 1σ confidence region in the N-T-n 3-dimensional space at the velocities where $\chi^2_{\rm red} \sim 1$ as the representative uncertainties of the fitted parameters. The uncertainties of CO column densities are ~ 10 %. The 1σ confidence ranges of temperatures are about 40 K - 60 K. At 50 K, the critical density of the CO (2-1), (3-2), (6-5) and (7-6) lines are 9×10^3 cm^{-3}, 3×10^4 cm^{-3}, 3×10^5 cm^{-3} and 4×10^5 cm^{-3}, respectively. The lower limits of gas

density derived from the LVG analysis are $\sim 10^5$ cm^{-3}, higher than or similar to the critical density of each line. The modeling results predict that the four transitions are optically thin in the outflowing gas, which is consistent with our assumptions. Figure A1 shows the comparison of the observed CO intensities with the LVG modeling results in each velocity bin.

3.2.4. *T-V and N-V relations*

Figure 5 shows the gas temperature and the CO column density of the G240 outflow as functions of the gas velocity, derived from the rotation diagram analysis and the LVG analysis. The N-V diagram shows a clear decreasing trend of CO column density with out-
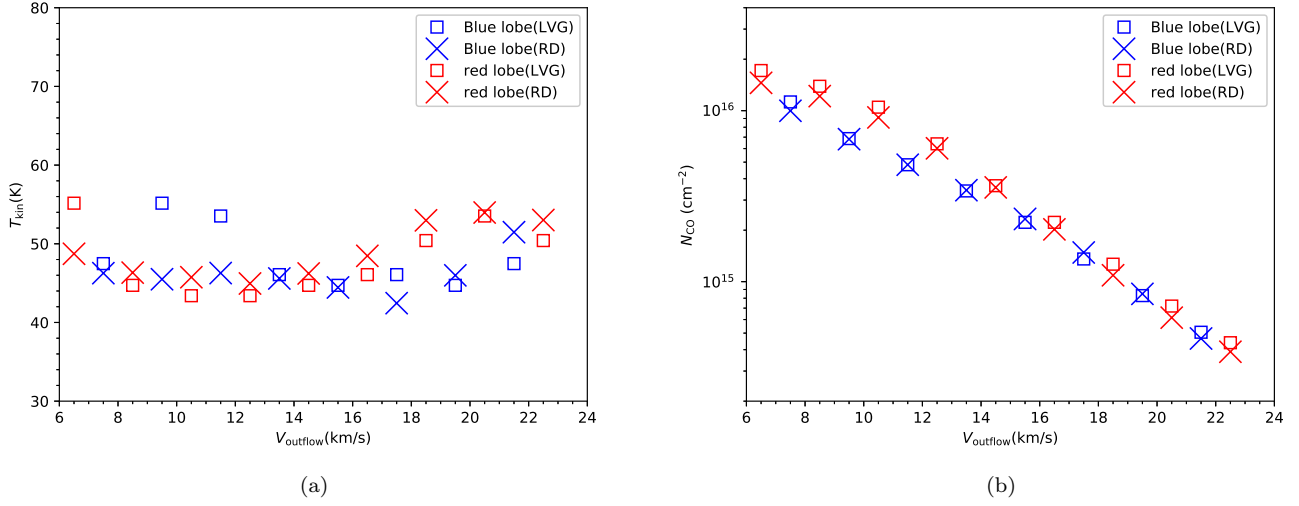
Figure 5. T-V and N-V diagrams of the G240 outflow, estimated from the rotation diagram analysis (blue x marker for the blue lobe and red x marker for the red lobe) and the LVG analysis (blue open squares for the blue lobe and red open squares for the red lobe).

flow velocity, while the T-V diagram shows that the gas temperature has no obvious dependence on gas velocity. We reran the rotation diagram analysis and the LVG analysis on line intensities measured at several different positions, and similar line ratios and modeling results with Figure 2 and Figure 5 were found. Thus, the systematic bias of position offsets was excluded.

4. DISCUSSION

4.1. *Gas temperature*

Though the morphology and kinematics of molecular outflows have been widely studied, some other physical properties (e.g., the variation of temperatures and densities with the outflow velocity and distance to the source) of molecular outflows are still unclear. In addition, studies on the the T-V relation of molecular outflows are very few. Based on constant CO 3-2/6-5 ratios, Yıldız et al. (2012) suggested that there is little or no temperature change with velocity in the outflow associated with low-mass protostars NGC 1333 IRAS 4A and 4B. With CO (2-1) and CO (3-2) observations, Su et al. (2012) performed an LVG analysis on the extremely high velocity outflow associated with the high-mass star-forming region G5.89-0.39 and found an increasing trend of temperature with outflow velocity. To infer the T-V relations from only two CO lines, they had to make assumptions of some other outflow parameters (e.g. gas density, canonical CO fractional abundance and velocity gradient). However, these assumptions might not be necessarily valid. To determine the outflow properties with better accuracy, multi-line CO studies with sophis-

ticated radiative transfer methods (e.g. LVG analysis) are required. Recently, Lefloch et al. (2015) performed a multi-transition CO study of the outflow cavity of the intermediate-mass Class 0 protostar Cepheus E-mm and revealed an isothermal low-excitation outflow with transitions of $J_{up} \leq 9$. Our analysis reveal that the G240 outflow, which is representative of a well-defined bipolar wide-angle molecular outflow in a $> 10^4 L_\odot$ star-forming region (Qiu et al. 2009), is isothermal and has a temperature of ~ 50 K. The isothermal state is in agreement with outflows (traced by transitions of $J_{up} \leq 9$) of low-mass protostars and intermediate-mass protostars (Yıldız et al. 2012; Lefloch et al. 2015), and the temperature value of ~ 50 K is consistent with temperatures in excess of 50 K probed by van Kempen et al. (2016) for outflows associated with intermediate-mass protostars, and slightly lower than temperatures of outflows associated with low-mass protostars (van Kempen et al. 2009a; Yıldız et al. 2012). Since the derived outflow temperature of ~ 50 K is warmer than previously adopted ~ 30 K (Qiu et al. 2009), the physical parameters (mass, momentum, energy) of the G240 outflow calculated by Qiu et al. (2009) were underestimated by a factor of 1.32.

4.2. *Gas density and CO column density*

The beam-averaged CO column density in each 2 km s^{-1} bin decreases from $\sim 2 \times 10^{16}$ cm^{-2} to $\sim 4 \times 10^{14}$ cm^{-2} within the outflow velocity range from $\sim \pm 7$ km s^{-1} to $\sim \pm 22$ km s^{-1} with respect to the cloud velocity. In the optically thin case, the beam-averaged CO column density N_{CO} is related to the gas density n_{H_2}

through the expression:

$$N_{\mathrm{CO}} = n_{\mathrm{H_2}} \times \Delta V \times \frac{1}{dv/dr} \times X_{\mathrm{CO}} \times f_{\mathrm{b}}, \qquad (2)$$

where f_{b} is the beam filling factor, X_{CO} the $[\mathrm{CO}]/[\mathrm{H_2}]$ abundance ratio, ΔV the velocity interval and dv/dr is the velocity gradient. The CO culumn density is degenerated with the beam filling factor, the velocity gradient and the abundance ratio. Since we didn't correct our observed line intensities with beam filling factors, the derived CO column densities in each velocity bin should be considered as lower limits. As shown in Figure 3 of Qiu et al. (2009), the source size are $\sim 20''$ and $\sim 10''$ at $\sim \pm 7$ km s^{-1} and $\sim \pm 22$ km s^{-1} with respect to the cloud velocity, corresponding to beam filling factors of ~ 0.5 and ~ 0.2, respectively. From the lowest velocities to the highest velocities of the outflowing gas, the beam-averaged CO column density has decreased 50 times, whereas the beam filling factor has only decreased 2.5 times. So one or serveral of these parameters ($n_{\mathrm{H_2}}$, dv/dr and X_{CO}) degenerated with the CO culumn density must have decreased with outflow velocity. Due to the lack of further informations, it is unclear whether the CO abundance ratio or the velocity gradient has attributed to the decrease of CO column density at higher velocities. If we assume the CO abundance ratio and the velocity gradient to be constant, the decrease of CO column density could be interpreted by a decrease of gas density with velocity.

4.3. *The origin of the G240 outflow*

A simple wide-angle wind-driven model predicts that the gas temperature of the outflow is relatively constant, and the outflow density decreases with velocity and distance from the driving source, while different trends are predicted by other outflow models (Arce et al. 2007). The estimated isothermal state and decreasing density-velocity trend of the G240 outflow agrees with the prediction of the wind-driven model. As the kinematics and morphology of the G240 outflow can also be qualitatively interpreted by the wide-angle wind-driven model (Qiu et al. 2009), we conclude that the wide-angle wind entrainment is the dominant driving mechanism of the G240 outflow. Since wide-angle winds (X-wind or disk winds) associated with low-mass YSOs are accretion driven (Shang et al. 2006; Pudritz et al. 2006), our analysing results support the scenario that high-mass stars up to late-O types can form via disk-mediated accretion. We noticed that there are faint bow-shaped H$_2$ features near the source IRAS 07427-2400 (Kumar et al. 2002), indicating that jet bow shock entrainment may also contribute to the G240 outflow. Mid-J CO observations with higher resolution (e.g. ALMA) are needed to study these suspicious bow shock features in detail. It should be noted that most existing outflow models have typical parameters of outflows driven by low-mass YSOs. High-mass outflow models are necessary to quantitatively explain the physical conditions of outflows of high-mass sources. Statics of massive outflows associated with high-mass star-forming regions are also essential for us to better understand the driven mechanism of massive outflows and the forming process of high-mass stars.

5. SUMMARY

We have presented the first CO multi-transition (CO 2-1, 3-2, 6-5, 7-6) study towards the molecular outflow of the high-mass star-forming region G240. The morphologies seen in the emission maps of four lines are very similar. The line ratios of the four transitions are remarkably constant with the outflow velocity. With the LVG analysis, we have constrained the temperatures to ~ 50 K and found a decreasing trend of CO column density with gas velocity. We also constrain the H$_2$ density to values higher than $n \sim 10^5$ cm^{-3} and found that the outflowing gas is thermalized. With the RD analysis, we found similar results of the LVG analysis in the temperature and the CO column density. The T-V relation of the G240 outflow agrees well with the wide-angle wind-driven model. Assuming a constant CO abundance ratio and a constant velocity gradient, we detect a decreasing gas density with velocity. A decreasing gas density with velocity is also consistent with the wide-angle wind-driven model. We conclude that the wide-angle wind-driven entrainment is the dominant driving mechanism of the G240 outflow. This finding indicate that disk-accretion can be responsible for the formation of high-mass stars even more massive than early B-type stars.

REFERENCES

Arce, H. G., Shepherd, D., Gueth, F., et al. 2007, Protostars and Planets V, 245

Banerjee, R., & Pudritz, R. E. 2006, ApJ, 641, 949

Beuther, H., Schilke, P., Sridharan, T. K., et al. 2002, A&A, 383, 892

Beuther, H., Schilke, P., Gueth, F., et al. 2002, A&A, 387, 931

Caswell, J. L. 1997, MNRAS, 289, 203

Caswell, J. L. 2003, MNRAS, 341, 551

Frank, A., Ray, T. P., Cabrit, S., et al. 2014, Protostars and Planets VI, 451

Goldsmith, P. F., & Langer, W. D. 1999, ApJ, 517, 209

Hughes, V. A., & MacLeod, G. C. 1993, AJ, 105, 1495

Kumar, M. S. N., Bachiller, R., & Davis, C. J. 2002, ApJ, 576, 313

Kumar, M. S. N., Fernandes, A. J. L., Hunter, T. R., Davis, C. J., & Kurtz, S. 2003, A&A, 412, 175

Lee, C.-F., Mundy, L. G., Reipurth, B., Ostriker, E. C., & Stone, J. M. 2000, ApJ, 542, 925

Lee, C.-F., Stone, J. M., Ostriker, E. C., & Mundy, L. G. 2001, ApJ, 557, 429

Lee, C.-F., Mundy, L. G., Stone, J. M., & Ostriker, E. C. 2002, ApJ, 576, 294

Lefloch, B., Gusdorf, A., Codella, C., et al. 2015, A&A, 581, A4

Machida, M. N., Inutsuka, S.-i., & Matsumoto, T. 2008, ApJ, 676, 1088-1108

MacLeod, G. C., Scalise, E., Jr., Saedt, S., Galt, J. A., & Gaylard, M. J. 1998, AJ, 116, 1897

Masson, C. R., & Chernin, L. M. 1993, ApJ, 414, 230

Maud, L. T., Moore, T. J. T., Lumsden, S. L., et al. 2015, MNRAS, 453, 645

Migenes, V., Horiuchi, S., Slysh, V. I., et al. 1999, ApJS, 123, 487

Pudritz, R. E., Rogers, C. S., & Ouyed, R. 2006, MNRAS, 365, 1131

Pudritz, R. E., Ouyed, R., Fendt, C., & Brandenburg, A. 2007, Protostars and Planets V, 277

Qiu, K., Zhang, Q., Wu, J., & Chen, H.-R. 2009, ApJ, 696, 66

Qiu, K., Zhang, Q., Menten, K. M., et al. 2014, ApJL, 794, L18

Raga, A., & Cabrit, S. 1993, A&A, 278, 267

Ren, J. Z., Liu, T., Wu, Y., & Li, L. 2011, MNRAS, 415, L49

Sakai, N., Nakanishi, H., Matsuo, M., et al. 2015, PASJ, 67, 69

Shang, H., Allen, A., Li, Z.-Y., et al. 2006, ApJ, 649, 845

Shepherd, D. S., Watson, A. M., Sargent, A. I., & Churchwell, E. 1998, ApJ, 507, 861

Shu, F. H., Ruden, S. P., Lada, C. J., & Lizano, S. 1991, ApJL, 370, L31

Shu, F. H., Najita, J. R., Shang, H., & Li, Z.-Y. 2000, Protostars and Planets IV, 789

Su, Y.-N., Liu, S.-Y., Chen, H.-R., & Tang, Y.-W. 2012, ApJL, 744, L26

Trinidad, M. A. 2011, AJ, 142, 147

van der Tak, F. F. S., Black, J. H., Schöier, F. L., Jansen, D. J., & van Dishoeck, E. F. 2007, A&A, 468, 627

van Kempen, T. A., van Dishoeck, E. F., Güsten, R., et al. 2009, A&A, 501, 633

van Kempen, T. A., van Dishoeck, E. F., Güsten, R., et al. 2009, A&A, 507, 1425

van Kempen, T. A., Hogerheijde, M. R., van Dishoeck, E. F., et al. 2016, A&A, 587, A17

Wu, Y., Wei, Y., Zhao, M., et al. 2004, A&A, 426, 503

Wu, Y., Zhang, Q., Chen, H., et al. 2005, AJ, 129, 330

Yıldız, U. A., Kristensen, L. E., van Dishoeck, E. F., et al. 2012, A&A, 542, A86

Zhang, Q., Hunter, T. R., Brand, J., et al. 2001, ApJL, 552, L167

APPENDIX

A. SPECTRAL LINE FLUX DISTRIBUTIONS
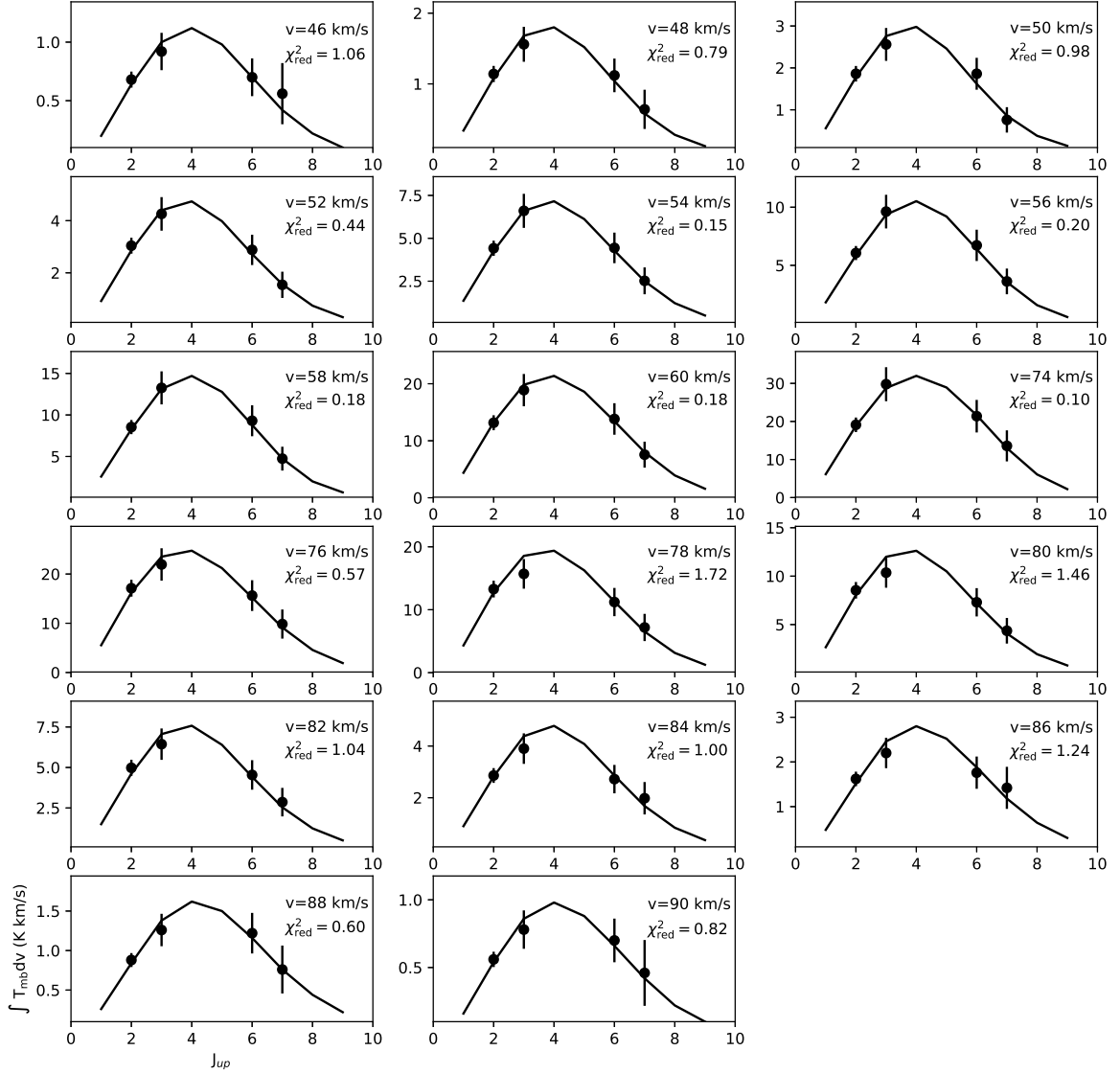
Figure A1. Observed line fluxes compared with the LVG computations in each 2 km/s bin. The black solid circles show the observed data with error bars. The black solid lines refer to the best fits. The $\chi^2_{\rm red}$ of the best fitting results and the outflow velocities are shown in each panel.